CHAPTER IV

STUDY ON THE X-RAY CALIBRATION AND OVERLAP MEASUREMENTS IN ROBOT-FORMED FLAKEBOARD MATS[*]

Abstract

An X-ray based experimental study is presented for determining the overlaps and horizontal density distribution (HDD) in robot-formed wood flakeboard mats. The relationship between overlaps and the X-ray intensity ratio has been developed. The results show that the calibration materials have little effect on the overlaps obtained from X-ray scanning and the estimated overlaps highly agree with those from computer simulations. Robot formed flakeboard mats have higher repeatability with lower deviation in both overlaps distribution and HDD than hand-formed mats.

4.1. Introduction

Several papers were recently published discussing the modeling and simulation of flakeboard mats. Steiner and Dai (1993) developed a rationale for predicting the spatial structure of wood composites in relation to processing and performance characteristics. Following the studies of paper formation (Kallmes *et al*. 1960, 1961 and 1963, Dodson 1971), a two-dimensional model based on the Poisson probability theory was set up to determine the flake

[*] A paper prepared from this chapter has been published in the Wood Science and Technology, 1999, 33(2): 85-95.

center distribution, flake overlap distribution, and HDD distribution in randomly formed mats (Dai and Steiner 1993, 1994a, 1994b and 1994c). Lang and Wolcott (1996) reported a model for viscoelastic consolidation of wood-strand mats through Monte Carlo simulation. These findings set up the foundation to characterize the structure of wood flake mats.

However, experimental measurement techniques needed to determine the physical characteristics of flakeboard still pose a challenge in future model development especially in the determination of HDD and overlaps in the mat area. The traditional gravimetric method to measure HDD in a mat by drilling or cutting (Xu and Steiner, 1995) is an extremely time-consuming and tedious procedure and it is impossible to get the same level of detail as the information available from computer simulation studies. The accuracy of the gravimetric technique is another factor of concern.

Soft X-ray scanning technology, which is one of the nondestructive testing methods that could be applied to a flakeboard mat, is a promising approach for detecting physically based factors relating to structures, such as voids and overlaps. Luggage inspection systems commonly found at airports are examples of applications of soft X-ray in which 2-dimensional line-scans are used. To date no literature has been found on the use of X-ray scanning for measuring HDD and overlaps in flakeboard mats.

This studies presents an X-ray calibration method and measurement techniques for determining the X-ray intensities and overlaps of flakeboard mats based on the principle of scaling of X-ray attenuation to flake overlaps. Robot forming techniques have also been used to obtain samples with known structures and high repeatability.

4.2. X-ray Theory and Overlap Model

4.2.1. X-ray theory and calibration

Beer's Law can be used to describe the X-ray absorption process in the scanned images. The value at any position defined by coordinate (x, y) in the mat area is given by the intensity $I_{(x,y)}$:

$$I_{(x,y)} = I_0 \cdot e^{-mtr_{(x,y)}} \tag{4.1}$$

where I_0 = the intensity of the incident radiation,

m = the X-ray mass absorption coefficient (cm^2/g),

t = the panel thickness in which X-ray traversed (cm), and

$r_{(x,y)}$ = the panel density (g/cm^3).

The X-ray scanning system consists of a soft X-ray source, a collimator, and a line array of detectors. What we get from X-ray scanning is the raw data (voltage levels) measured by the detectors which are meaningless unless properly calibrated. The X-ray system was calibrated with three aluminum plates (thickness for each plate 1.521 mm / density 2.700 g/cm^3) and three plexiglas (methyl methacrylate) plates (thickness of each plate 9.286 mm / density 1.194 g/cm^3). Within each material, four image files containing the voltage levels of X-ray absorption characteristics for each pixel were obtained by placing three, two, one and zero plates in between the X-ray source and the detectors. The curve fitting program takes these four images and averages all the values for each pixel in each file, then simultaneously solves the equations to obtain four coefficients (a_0, a_1, a_2, a_3) for a best fit third order curve:

$$a_0 + a_1 v + a_2 v^2 + a_3 v^3 = I \tag{4.2}$$

where v = values in the scanned images (voltage levels),

a_0, a_1, a_2, a_3 = the cubic coefficients, and

I = the intensity of the X-ray scanning.

If we assume that the thickness (t) and the density (r) are uniform within each plate, then the X-ray intensity (I) reduces to $k_i I_0$, where the subscript i = 0, 1, 2, 3 denotes the case which X-ray goes through zero, one, two and three plates, respectively and the k_i is the scaling factor. During the calibration period, the coordinate y was kept constant; thus

$$k_i = e^{-u t_i r} \tag{4.3}$$

For zero plate ($t_0 = 0$),

$$k_0 = e^{-m t_0 r} = 1.0 \tag{4.4a}$$

For one, two and three plates cases, the k_1, k_2, and k_3 are evaluated by the following equations:

$$k_1 = e^{-m t_1 r} \tag{4.4b}$$

$$k_2 = e^{-m t_2 r} = k_1^2 \tag{4.4c}$$

$$k_3 = e^{-m t_3 r} = k_1^3 \tag{4.4d}$$

where $t_2 = 2t_1$ and $t_3 = 3t_1$

Therefore, the four coefficients (a_0, a_1, a_2, a_3) can be solved as a function of I_0. The intensity ratio **(I_0/I)** will be used throughout the subsequent discussion.

4.2.2. Mass absorption coefficient

The mass absorption coefficient, m, consists of three components, the photoelectric effect, m_e, the Compton scattering effect, m_c, and the pair production effect, m_p, *i.e.*

$$m = m_e + m_c + m_p \tag{4.5}$$

At relative low energies (photon energy $\leq$ 1.02 MeV (Selman 1994)), m is mainly a mixture of photoelectric with Compton interactions. Cho (1975) and Tsai (1976) developed a model for calculating these coefficients and Lindgren (1991) successfully utilized this model to obtain the linear absorption coefficients for wood constituents at 73 keV. From their studies, the mass absorption coefficients can be summarized as follows:

$$m_1 = m_e + m_c = k_1 \frac{N\tilde{Z}^m}{AE^{3.1}} + k_2 \frac{N\tilde{Z}}{A} f(E) \tag{4.6a}$$

$$m_2 = m_e + m_c = k_1 \frac{n_0\tilde{Z}^{m-1}}{E^{3.1}} + k_2 n_0 f(E) \tag{4.6b}$$

where m_1 is the mass absorption coefficient for single element, m_2 is the mass absorption coefficient for compound substances, k_1 and k_2 are constants, n_0 is the electron density (electron/g), A is the atomic weight, $\tilde{Z}$ is the effective atomic number, N is the Avogadro's number, m is a constant which equals to 4.4 for all biological substances, and the E is the energy of the incident photon in keV. According to Selman (1994), an X-ray beam having a

particular kVp (peek voltage) has a quality resembling a monoenergetic X-ray beam of about one-third to one-half the peak energy, *i.e.*, the maximum monoenergetic X-ray energy for 74 kVp is 37 keV.

The effective atomic number $\tilde{Z}$ and the electron density n_0 can be obtained according to the following equations:

$$\tilde{Z} = \left(\sum \alpha_i Z_i^{3.4} \right)^{\frac{1}{3.4}} \tag{4.7}$$

$$n_0 = N \sum (P_i Z_i / A_i) \tag{4.8}$$

and

$$\alpha_i = \frac{P_i Z_i / A_i}{\sum (P_j Z_j / A_j)} \tag{4.9}$$

where α_i is the relative electron fraction of element i, and P_i is the percentage weight of element i. $f(E)$ is a function of photon energy E, which can be expressed as:

$$f(E) = \frac{1+\beta}{\beta^2}\left(\frac{2(1+\beta)}{1+2\beta} - \frac{\ln(1+2\beta)}{\beta}\right) + \frac{\ln(1+2\beta)}{2\beta} - \frac{1+3\beta}{(1+2\beta)^2} \tag{4.10}$$

where $\beta = E/511$.

The above equations (Cho 1975) make it possible to calculate the mass absorption coefficient for any material as long as its chemical composition is known. According to Fengel and Wegener (1984), aspen (*Populus tremuloides*) consists of about 42.7% cellulose, 36.0% hemicellulose, 20.9% lignin and 0.4% ash on an extractive-free basis. The cellulose,

hemicellulose and lignin can be chemically regarded as $C_6H_{10}O_5$, $C_{5.3}H_{7.0}O_{4.6}$, and $C_{10}H_{13}O_2$, respectively. The calculated mass absorption coefficients for aluminum, plexiglas and aspen are tabulated in **Table** 4.1.

Table 4.1. Calculated mass absorption coefficients

Substances	Chemical formula	Volume fraction (%)	m
Aluminum	Al	100	0.6400
Plexiglas	$C_5H_8O_2$	100	0.2391
Aspen			0.2395
Cellulose	$C_6H_{10}O_5$	42.7	0.2489
Hemicellulose	$C_{5.3}H_{7.0}O_{4.6}$	36.0	0.2441
Lignin	$C_{10}H_{13}O_2$	20.9	0.2169

4.2.3. Relationship between overlaps and intensity ratio (I_0/I)

Equation 4.1 can be rewritten as

$$r_{(x,y)} = \frac{1}{mt} ln(\frac{I_0}{I_{(x,y)}}) = \frac{1}{mt} ln(k_{(x,y)}) \tag{4.11}$$

where $k_{(x,y)}$ = the intensity ratio **($I_0/I_{(x,y)}$)**.

The mass in a unit area in the panel equals to $\tau_{(x,y)}$. It is also equal to the total flake height $O_{(x,y)}t_f$ times flake density ρ_f. In mathematical form, it is

$$\tau_{(x,y)} = O_{(x,y)} t_f \rho_f \tag{4.12}$$

where $O_{(x,y)}$ = overlaps in a unit area,

t_f = flake thickness, and

ρ_f = flake density.

Therefore, the overlaps have the following relationship with X-ray intensity ratio, flake thickness and density

$$O_{(x,y)} = \frac{1}{\mu t_f \rho_f} \ln(k_{(x,y)}) = \frac{\rho_{(x,y)} t}{t_f \rho_f} \tag{4.13}$$

It is evident that the number of flake overlaps has a linear relationship with panel density. Therefore, the flake overlap distribution within the mat can represent density distribution in the horizontal plane.

4.2.4. Image filter

The application of a binomial filter is needed to remove the undesirable random noise during X-ray scanning and to smoothen the sharp points in the images. The values for the coefficients of an odd-sized binomial mask can be expressed directly using the following binomial distribution with mean of Qp and variance of $Qp(1 - p)$ (Bernd 1991).

$$p_q = \frac{Q!}{q!(Q-q)!} p^q (1-p)^{Q-q} \tag{4.14}$$

Where Q denotes the order of binomial levels, for p = ½, the above equation becomes

$$p_q = \frac{1}{2^Q} \frac{Q!}{q!(Q-q)!} \tag{4.15}$$

When the order of the binomial Q = 2, the filter mask is ¼[1 2 1]. The smallest mask of this kind in two-dimensional is a 3 × 3 binomial filter. The application of 3 × 3 binomial filter is referred to by Bernd (1991).

4.3. Materials and Methods

Two different structures of 250mm × 250mm testing panels were prepared using phenol-formaldehyde resin powder (**Figure** 4.1). Uniform aspen flakes (measured average density 0.435 g/cm^3) were used with the dimension of 75 mm length, 19.1 mm width, and 0.61 mm thickness in Structure I (Wang and Lam 1998) and 100 mm × 20 mm × 0.72 mm in Structure II. Flake centroid positions in the mat area ($0 \le x \le 250$, $0 \le y \le 250$) are randomly generated based on the Poisson distribution for both structures of mats. All the flakes are perfectly aligned in each layer in Structure I with 90^o in two adjacent layers and completely randomized flake orientation in Structure II. The robot forming techniques have been applied to obtain samples with the above-defined structures. The flake position (x, y) and orientation angles (q) are the inputs for a robot driver program to form the experimental mat.

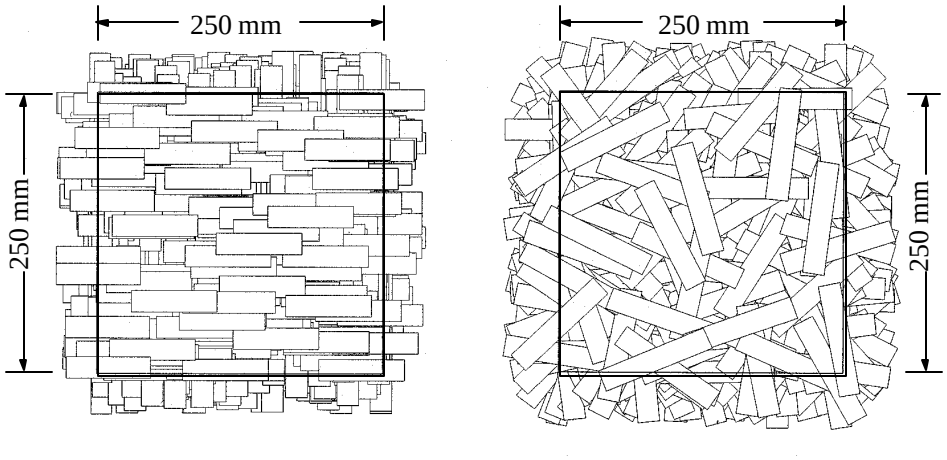

Structure I: Defined orientations and random positions

Structure II: Completely randomized orientations and positions

Figure 4.1 Schematic representation of the mat structures.

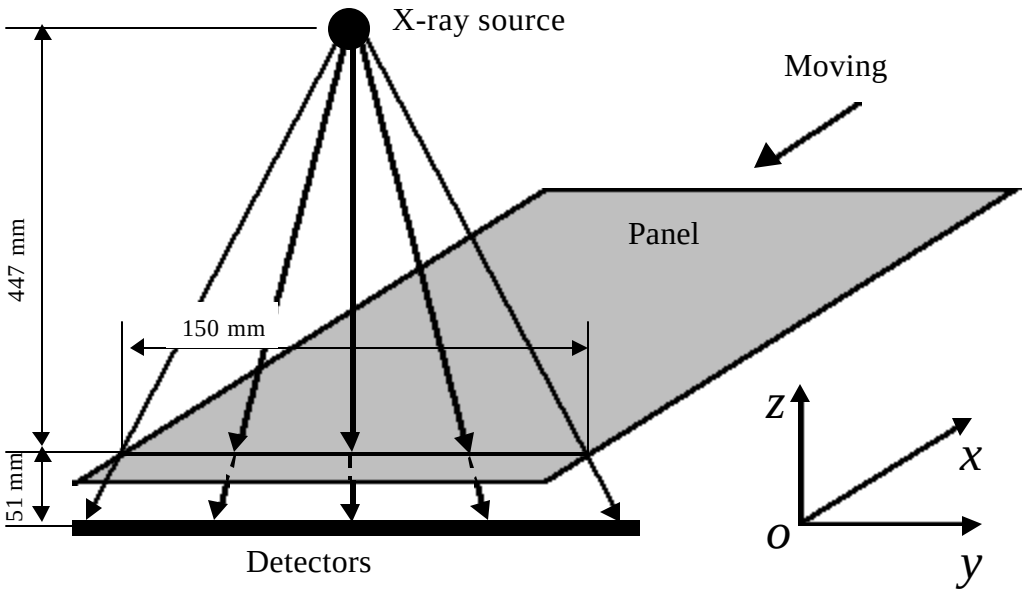

Figure 4.2 Schematic diagram of the X-ray scanning system.

During X-ray scanning, the distance between any two adjacent scans was selected as small as 2 mm in x direction. The X-ray attenuation profile, $P(y)$, on the y axis is a function of cumulative X-ray absorption with X-rays projected normally to that axis in the z direction (**Figure** 4.2). As the panel moves along the x axis (X-ray source and detectors fixed) in the scanning process, the attenuation profile becomes two-dimensional. $P(x, y)$ is then typically digitized in the resolution of 1.5mm × 2mm. The image analysis techniques mentioned above are applied to extract signals which could be used to characterize the presence of overlaps or/and voids in the panel.

4.4. Results and Discussions

4.4.1. X-ray calibration

Two steps are used to obtain the flake overlaps from the X-ray images. First, the raw scanned (voltage levels) images were converted to X-ray intensity images by fitting the third order curve given in **Equation** 4.1. Then panel density and flake overlaps in the position (x, y) in the mat area can be obtained from the **Equations** 4.11 and 4.13.

The scaling factors k_i (i = 0, 1, 2, 3) used in the curve fitting process obtained from considering the X-ray absorbed by the two kinds of calibration materials (aluminum and plexiglas) are tabulated in **Table** 4.2. When there is no plate between the X-ray source and the detectors, the scaling factor is 1.0 for intensity which can be regarded as the incident radiation (I_0) detected by the X-ray system and constant for both calibration materials. Since the flake overlaps are fixed at the location (x, y), the converted X-ray intensity ratio (I_0/I)

should also be kept constant no matter what material was used in the calibration. However, due to the different voltage levels obtained from the two materials, we could not expect the calibration coefficients (a_0, a_1, a_2, a_3) (**Table** 4.3) to be the same for both cases. In single byte storage (range from 0 to 255), the intensity ratio (I_0/I) decreases monotonically as the voltage level increases (**Figure** 4.3).

Table 4.2 Scaling factors for X-ray intensity under different number of calibration plates

No. of plates	0	1	2	3
Aluminum ($m = 0.6400$)	1.0000	0.7695	0.5921	0.4556
Plexiglas ($m = 0.2391$)	1.0000	0.7672	0.5886	0.4516

Table 4.3 Calibration coefficients for one pixel ($\times I_0$)

	a_0	a_1	a_2	a_3
Aluminum	0.1240	2.2429E-03	2.2688E-05	-6.5513E-08
Plexiglas	0.0556	4.4953E-03	1.9411E-06	-9.8752E-09

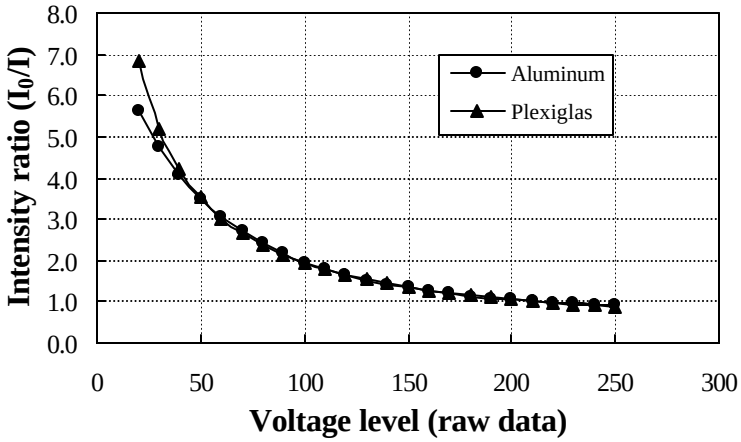

Figure 4.3 The relationship between X-ray intensity ratio and voltage levels.

4.4.2. Relationship between X-ray intensity ratio and flake overlaps

In order to verify the relationship between X-ray intensities and flake overlaps, another 6 measurements were made on the different flake stacks (5, 10, 15, 20, 25, and 30 flakes). The results are as shown in **Figure** 4.4. The experimental measurement is in good agreement with the model predicted. As stated in **Equation** 4.13, the overlaps are a function of natural logarithm of the inverse intensity. However, at small overlaps (less than 50) a linear relationship was observed between flake overlaps and the X-ray intensity ratio (**Figure** 4.4). The reason is from **Equation** 4.13,

$$k_{(x,y)} = e^{mt_f r_f O_{(x,y)}} \approx 1 + mt_f r_f O_{(x,y)} \tag{4.16}$$

for small values of $mt_f r_f O_{(x,y)}$.

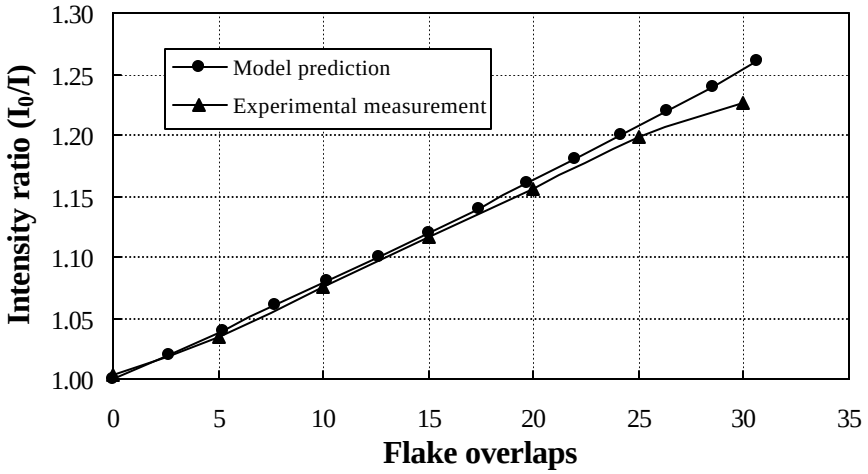

Figure 4.4 Flake overlaps in relation to X-ray intensity ratio

Hence, **Equation** 4.13 can be rewritten as:

$$O_{(x,y)} \approx \frac{k_{(x,y)} - 1}{mt_f r_f} \tag{4.17}$$

The commercial OSB panels with 10 mm thickness usually have less than 30 flakes in a column on average, while the laboratory made flakeboards have 24.5 flake overlaps for structure I and 21 flake overlaps for structure II. This will introduce an error in X-ray intensity ratio of 2.2% for commercial OSB panels and 1.1% - 1.5% for laboratory made samples by applying the approximation in **Equation** 4.17.

4.4.3. Flake overlaps from X-ray scanning images

Figure 4.5 shows the X-ray scanning images of density of three replicated robot-formed

panels and one simulated density image for each of the mat structures (**Figure** 4.1). Increase in darkness of the map denotes high density. The statistical results for flake overlaps are listed in **Table** 4.4. The simulated mats have higher standard deviation of the means due to higher resolution and accuracy. From the image pattern, the simulated mats match the experimental panels quite well and the three experimental panels in each structure have high repeatability. This means that few replications are required by using a robot in our experiment so that both time and costs will be reduced in the future studies. One particular scanning line from each of these images is drawn in **Figure** 4.6 for closer comparison. The variation of overlaps inside the panel at an arbitrarily scanning line agrees well with the simulation line at the same location.

The overlap information in 240mm × 240mm of mat area was extracted and subdivided into 144 sampling zones (20mm × 20mm) (see **Figure** 4.5) to investigate the variation of local overlap averages among these zones. As shown in **Figure** 4.7 (only the first 48 zones were plotted), the corresponding sampling zones vary accordingly. Therefore, a quantitative characterization of the overlaps may lead to predictions of the variability of panel properties by nondestructive testing method and simulation process.

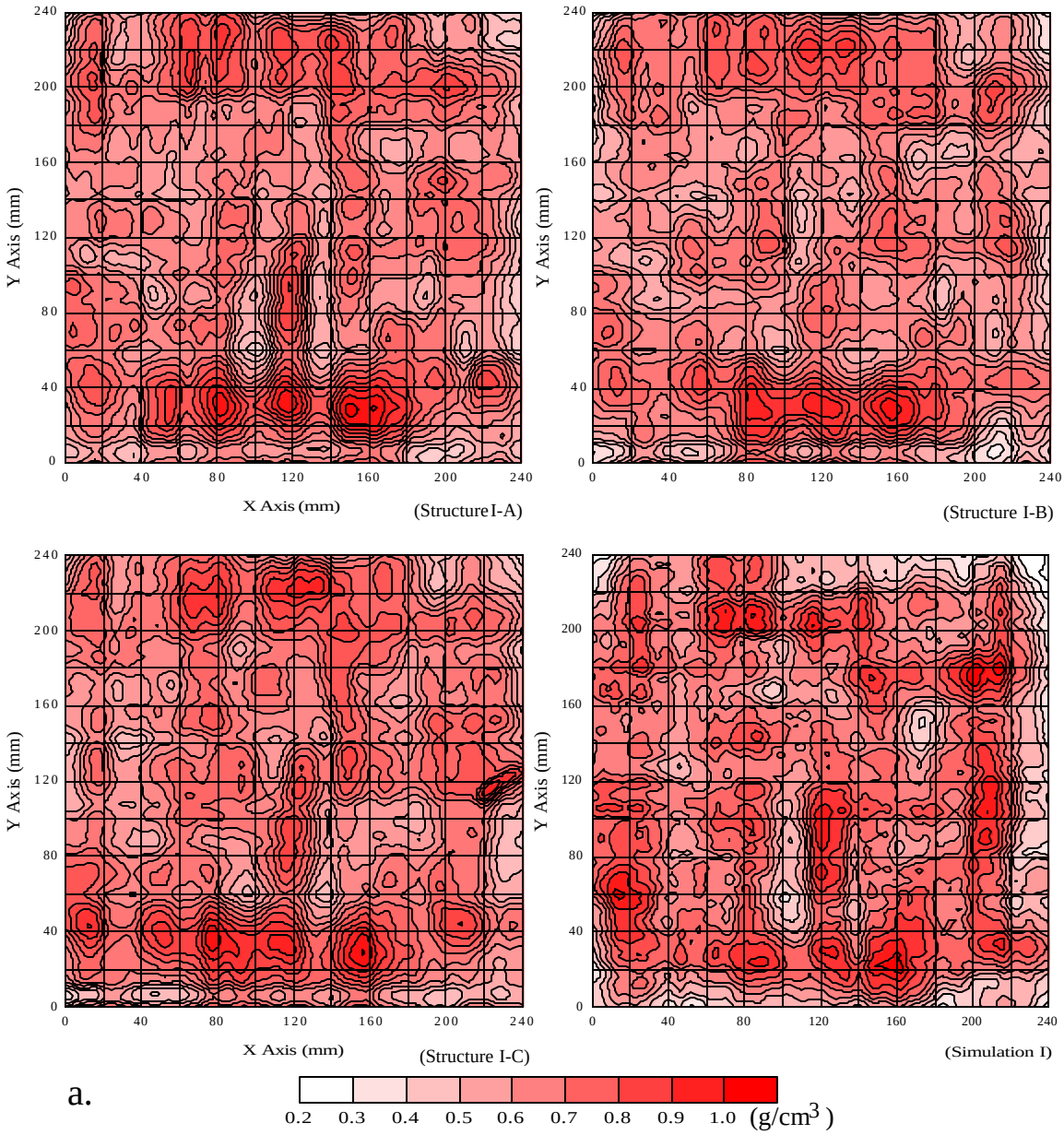

Figure 4.5a Horizontal density distribution images from X-ray measurements in Structure I.

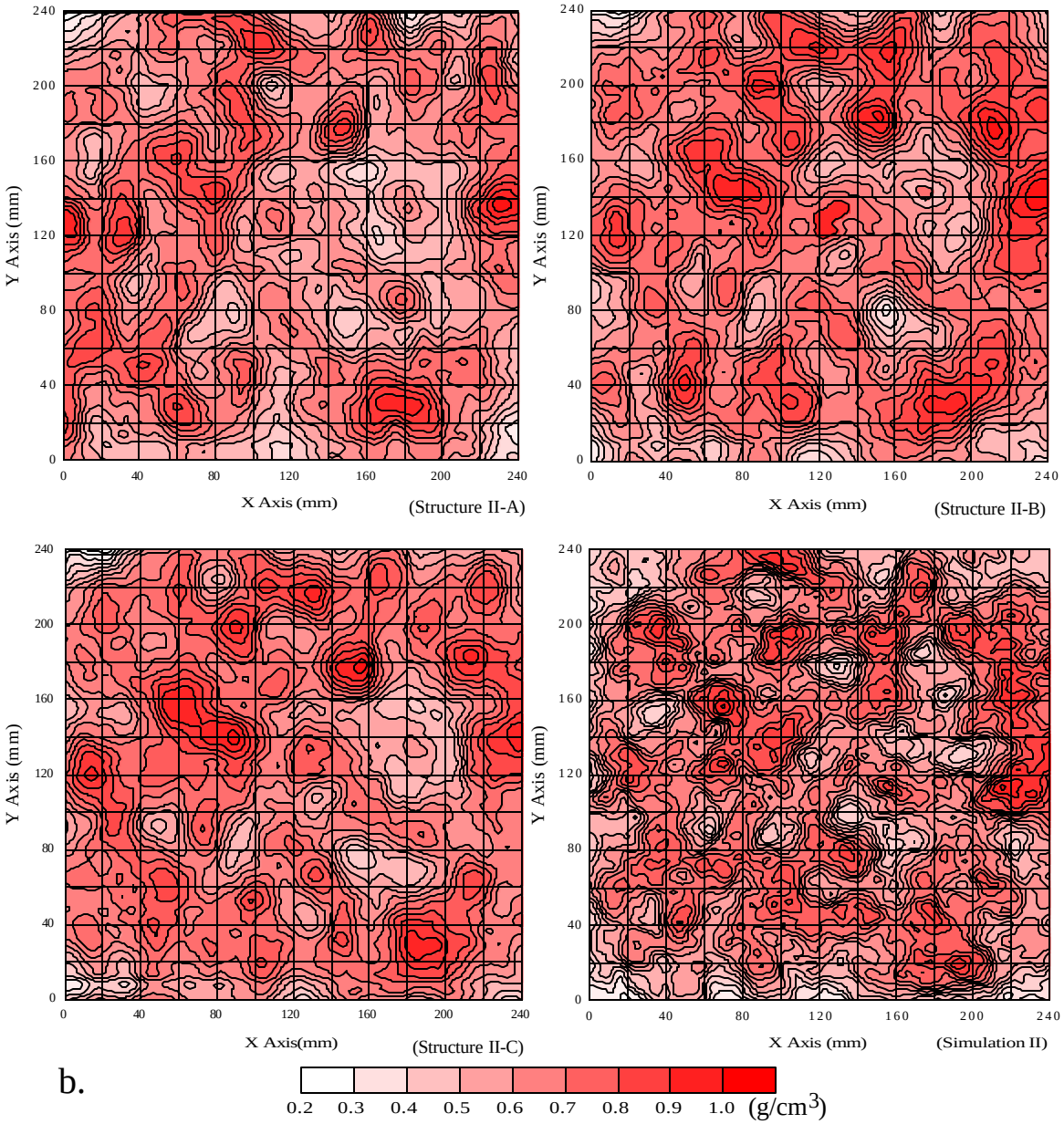

Figure 4.5b Horizontal density distribution images from X-ray measurements in Structure II.

Table 4.4 The statistical results from the X-ray analysis of three images (121 × 163 pixels) of each mat structure as compared to computer simulation

Source	Mean (overlap)	Maximum (overlap)	Minimum (overlap)	Std. dev. of the mean	Corrected density (g/cm^3)
Structure I-A	24.3	39.9	5.1	4.1	0.595
Structure I-B	23.1	36.7	4.8	4.3	0.565
Structure I-C	24.9	37.1	9.2	4.0	0.608
Simulation I	24.5	38.6	6.6	5.3	0.599
Structure II-A	19.3	30.4	6.3	3.4	0.552
Structure II-B	21.0	30.9	7.4	3.5	0.599
Structure II-C	20.7	30.2	5.9	3.3	0.591
Simulation II	21.1	33.3	8.4	4.2	0.609

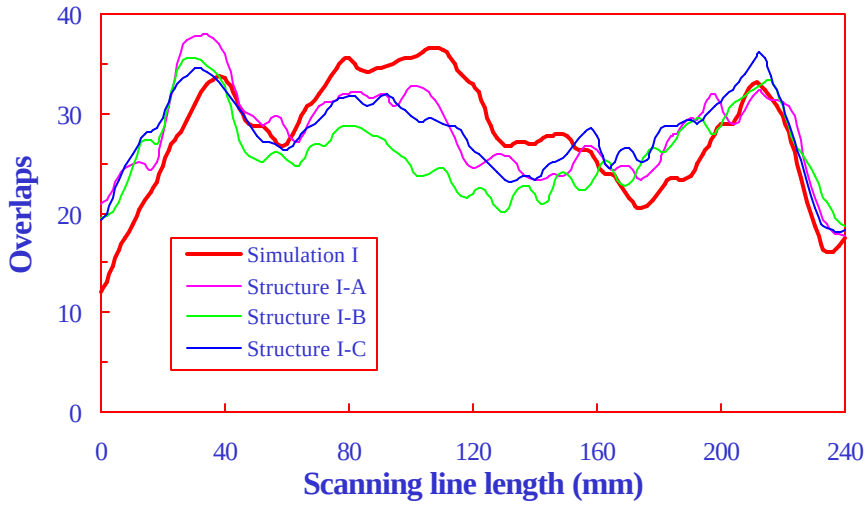

Figure 4.6 Flake overlaps in a particular scanning line in the mat area for the simulation and X-ray measurements in structure I.

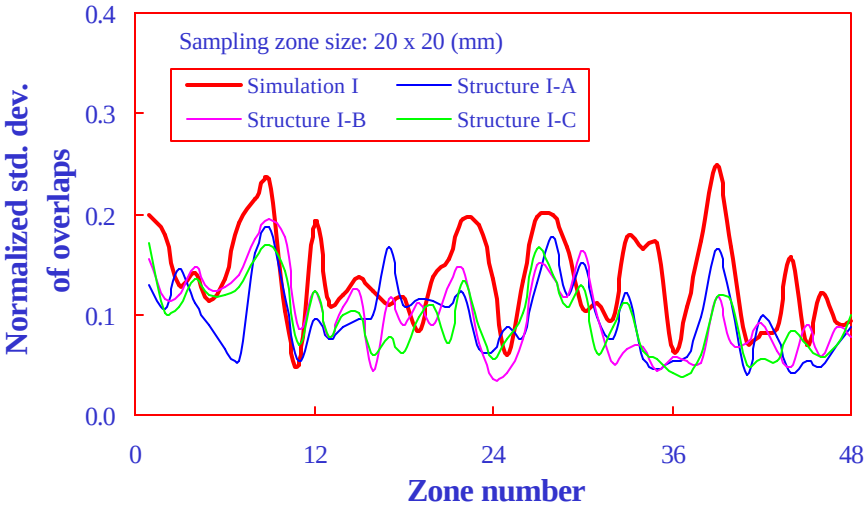

Figure 4.7 Comparing the normalized standard deviation of density for the simulation and X-ray measurements in structure I.

4.5. Conclusions

In modeling the overlaps and/or densities in the mat area, the mat is considered as a grouping of multi-stacked flake columns (Dai and Steiner, 1993). The overlap distribution contributes to the variation of the panel properties. This paper developed a model to predict the overlaps by an X-ray scanning method. A close relationship was found between number of overlaps and X-ray intensity ratio.

The results also show that the calibration materials have little effect on the number of overlaps obtained from X-ray scanning and the overlaps are in good agreement with those from computer simulations. The robot formed flakeboard mats have higher repeatability with lower deviation in both overlap distribution and horizontal density distribution. A robot can play an active role in reducing replications of the experiment in future studies.

4.6. References

Bernd, J. 1991. Digital Image Processing: Concepts, Algorithms and Scientific Applications. Springer-Verlag. Berlin

Cho, Z. H.; Tsai, C. M. and Wilson, G. 1975. Study of contrast and modulation mechanisms in X-ray/photon transverse axial transmission tomography. Phys. Med. Biol. 20(6): 879-889

Dai, C. and Steiner, P. R. 1993. Compression behavior of randomly formed wood flake mats. Wood and Fiber Science, 25(4):349-358

Dai, C. and Steiner, P. R. 1994a. Spatial structure of wood composites in relation to simulation of a randomly formed flake layer network. Part 2. Modeling and simulation of a randomly formed flake layer network. Wood Science and Technology, 28:135-146

Dai, C. and Steiner, P. R. 1994b. Spatial structure of wood composites in relation to processing and performance characteristics. Part 3. Modeling the formation of multi-layered random flake mats. Wood Science and Technology 28: 229-239

Dai, C. and Steiner, P. R. 1994c. Analysis and implication of structure in short fiber wood composites. Second Pacific Rim Bio-Based composites Symposium, Nov. 6-9, Vancouver, Canada, p17-24

Dodson, C.T.J. 1971. Spatial variability and the theory of sampling in random fibrous network. J. Roy. Statist. Soc. Series B. 33(1): 88-94

Fengel, D. and Wegener, G. 1984. Wood : Chemistry, Ultrastructure, Reactions. Berlin ; New York.

Kallmes, O. and Bernier, G. 1963. The structure of paper. IV. The free fiber length of a multiplanar sheet. Tappi 46(2): 108-114

Kallmes, O. and Corte, H. 1960. The structure of paper. I. The statistical geometry of an ideal two dimensional fiber network. Tappi 43(9): 737-752

Kallmes, O.; Corte, H. and Bernier, G. 1961. The structure of paper. II. The statistical geometry of a multiplanar fiber network. Tappi 44(7): 519-528

Lang, E. M. and Wolcott, M. P. 1996. A model for viscoelastic consolidation of wood-strand mats. Part I. Structural characterization of the mat via Monte Carlo simulation. Wood and Fiber Science 28(1): 100-109

Lindgren, L. O. 1991. Medical CAT-scanning: X-ray absorption coefficients, CT-numbers and their relation to wood density. Wood Science and Technology 25:341-349

Selman, J. 1994. The fundamentals of X-ray and radium physics. Eighth Edition. Charles C Thomas Publisher. Illinois, USA

Steiner, P. R. and Dai, C. 1993. Spatial structure of wood composites in relation to processing and performance characteristics. Part 1. Rationale for model development. Wood Science and Technology, 28: 45-51

Tsai, C. M. and Cho, Z. H. 1976. Physics of contrast mechanism and averaging effect of linear attenuation coefficients in a computerized transverse axial tomography (CTAT) transmission scanner. Phys. Med. Biol. 21(4): 544-559

Wang, K. and Lam, F. 1998. Robot-based research on a three-layered oriented flakeboard. Wood and Fiber Science, 30(4): 339-347

Xu, W. and Steiner, P. R. 1995. A statistical characterization of the horizontal density distribution in flakeboard. Wood Fiber Sci. 27(2): 160-167